

Contents lists available at ScienceDirect

Nano Today

journal homepage: www.elsevier.com/locate/nanotoday



Redox-driven mechanoregulation of invasive TNBC cells using poly(tannic acid) nanospheres

Minhee Ku^{a,b,1}, Suhui Jeong^{c,d,1}, Nara Yoon^a, Hwain Myeong^{c,d}, Jinwon Kwon^a, Jaemoon Yang^{a,b,*}, Sungbaek Seo^{c,d,**}

- ^a Department of Radiology, College of Medicine, Yonsei University, Seoul 03722, Republic of Korea
- ^b Convergence Research Center for Systems Molecular Radiological Science, Yonsei University, Seoul 03722, Republic of Korea
- ^c Department of Biomaterials Science (BK21 FOUR Program), College of Natural Resources and Life Science, Miryang 50463, Republic of Korea
- ^d Life and Industry Convergence Research Institute, Pusan National University, Miryang 50463, Republic of Korea

ARTICLE INFO

Keywords: Antioxidant Mechanoregulation Polyphenol nanoparticles Redox signalling Metastatic cancer cells

ABSTRACT

Poly(tannic acid) (pTA) nanospheres, assembled from natural tannic acid molecules, exhibit strong intracellular antioxidant activity and effectively modulate the invasive behaviour of triple-negative breast cancer (TNBC) cells. Acting as redox-active nanostructures, pTA nanospheres suppress proliferation and induce mechanoregulatory changes, including altered nuclear morphology, cytoskeletal disassembly, and diminished cell polarity. Specifically, pTA treatment causes spatial mislocalization of MT1-MMP from the invasive front to the perinuclear zone, disrupting its colocalization with F-actin and reducing its matrix-degrading capacity. High-resolution STED and TEM imaging reveal vimentin network collapse and mitochondrial redistribution along microtubules. Metabolic profiling shows a marked decline in oxidative phosphorylation-linked ATP production. Despite these functional disruptions, cleaved caspase-3 remains undetectable, indicating a non-apoptotic, cytostatic state accompanied by autophagy and redox signalling compensation. These findings demonstrate that pTA nanospheres exert redox-driven mechanoregulation in TNBC cells, limiting their invasive potential without inducing cell death, and highlight their promise as a non-lethal nanotherapeutics approach for post-surgical or adjuvant control of metastatic progression.

1. Introduction

Chemotherapy remains one of the primary clinical strategies for treating cancer; however, a major challenge is the persistence of residual tumour cells or carcinomatous tissue that survive initial treatment. These surviving cells often exhibit enhanced aggressiveness and metastatic potential, ultimately compromising therapeutic outcomes and contributing to cancer recurrence [1–5]. Current clinical practice addresses this issue by administering additional chemotherapeutic agents or incorporating adjuvants, such as immunopotentiators or reactive oxygen species (ROS) modulators, to either eliminate residual cancer cells or strengthen the immune response [6–8]. Antioxidants, in particular, have drawn attention as adjuvant agents capable of altering redox-sensitive signalling pathways and inducing apoptosis in tumour

cells by limiting lipid peroxidation and intracellular oxidative stress $\lceil 9-11 \rceil$.

To maximize the anti-metastatic potential of antioxidant adjuvants, we hypothesized that the molecular assembly of antioxidant units into nanoscale architectures could amplify their intracellular activity and enhance their delivery to target sites. Natural polyphenols are well known for their ROS-scavenging capability via hydrogen atom donation from their phenolic hydroxyl groups. In particular, tannic acid (TA), a hydrolysable polyphenol, has demonstrated environmental stability and sustained antioxidant activity, even under physiological stress [10]. In our previous study, the surface coating of TA onto nanocarriers resulted in the remodelling of cytoskeletal structures in cancer cells, suggesting a promising route for attenuating metastatic behaviour via redox modulation.

^{*} Corresponding author at: Department of Radiology, College of Medicine, Yonsei University, Seoul 03722, Republic of Korea.

^{**} Corresponding author at: Department of Biomaterials Science (BK21 FOUR Program), College of Natural Resources and Life Science, Miryang 50463, Republic of Korea.

E-mail addresses: 177hum@yuhs.ac (J. Yang), sbseo81@pusan.ac.kr (S. Seo).

 $^{^{1}\,}$ M.K. and S.J. contributed equally to this work.

Building on these findings, we developed poly(tannic acid) (pTA) nanospheres through resorcinol–formaldehyde-assisted polymerization, producing a self-assembled structure composed of multiple TA molecules per particle. This design not only enhances antioxidant potency but also improves cellular internalization efficiency due to the nanoscopic form factor (Fig. 1a). Unlike conventional polyphenol-based nanocarriers, which encapsulate or surface-immobilize polyphenols as releasable cargos, pTA nanospheres are structurally composed entirely of polymerized tannic acid. This configuration provides exceptionally high polyphenol content per nanoparticle, enabling sustained antioxidant activity and redox modulation. Importantly, this nanoplatform enables us to study the direct effects of polyphenol-based antioxidants on the cellular machinery of triple-negative breast cancer (TNBC), a subtype notorious for its invasive phenotype and lack of targeted therapies [12–15].

In this study, we systematically investigated how pTA nanospheres modulate redox homeostasis and its subsequent effects on cancer cell mechanoregulation, including migration and invasiveness (Fig. 1a).

Using MDA-MB-231 TNBC cells as a model, we performed highresolution, multiparametric analyses, including confocal and superresolution STED microscopy, live-cell metabolic assays, cytoskeletal and focal adhesion imaging, ECM degradation assays, and spatial mapping of MT1-MMP trafficking. The depth and resolution of our cellular investigations offer compelling evidence for the anti-metastatic potential of pTA nanospheres. Our work highlights the promise of nanostructured antioxidant systems as both redox modulators and effective mechanoregulators of cancer invasiveness, providing a material-driven strategy for next-generation cancer therapeutics.

2. Experimental section

2.1. Materials

Pluronic© F-127, formaldehyde solution (37 wt%) and phosphatebuffered saline (PBS, pH 7.2) were purchased from Sigma-Aldrich (St. Louis, MO, USA). TA was purchased from Alfa Aesar (Waltham, MA,

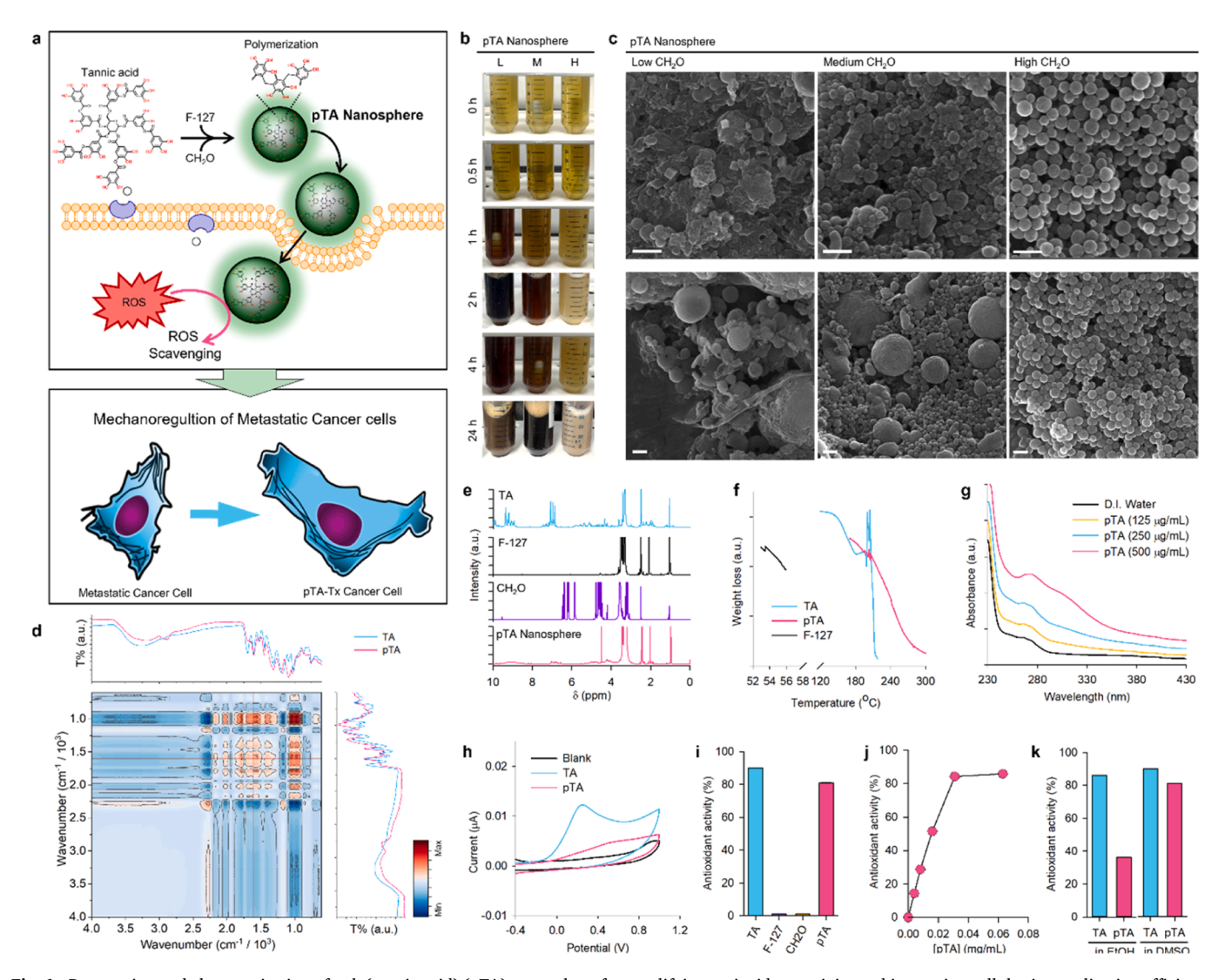


Fig. 1. Preparation and characterisation of poly(tannic acid) (pTA) nanosphere for amplifying antioxidant activity and improving cellular internalization efficiency. a Schematic illustration of pTA nanosphere formation via polymerization and its antioxidant and mechanoregulation effects. b Photographs of the pTA nanosphere reaction solutions prepared with three different concentrations of formaldehyde (CH₂O; Low L, Medium M, High H) taken at various time points (0, 0.5, 1, 2, 4, and 24 h). c SEM images for the prepared pTA nanospheres at the indicated conditions. Scale bars are 200 nm. d 2D FTIR correlated spectra for the TA and pTA nanosphere. e 1 H NMR spectra of the TA, F-127, formaldehyde, and pTA nanosphere. f Thermogravimetric analysis of TA, F-127, and pTA nanospheres. g UV-Vis absorbance spectra of pTA nanospheres. h Cyclic voltammetry (CV) analysis of TA and pTA nanospheres in chloroform. i Antioxidant activity of TA, F-127, ammonia, formaldehyde, and pTA nanosphere (n = 3). j Antioxidant activity of pTA nanosphere at different concentrations in DMSO by DPPH assay (n = 3). k Comparison of the antioxidant activity of TA and pTA sphere in ethanol and DMSO solution (n = 3).

USA). Ammonia solution (25 wt%), L(+)-ascorbic acid, and ethanol were purchased from Samchun Chemicals (Seoul, Republic of Korea). Tetrabutylammonium hexafluorophosphate was purchased from Sejin CI (Seoul, Republic of Korea).

2.2. Synthesis of poly(tannic acid) nanospheres

pTA nanospheres were synthesized by formaldehyde substitution crosslinking in ammonia base catalysts [16]. F-127 (0.1 g) was dissolved in a solvent mixed with distilled water (DI water) (24 mL) and ethanol (4 mL) containing a 25 wt% ammonia solution (0.25 mL), and the solution was stirred for 1 hr. Then, TA (0.2 g) was added to the above solution. After TA was completely dissolved, 37 wt% formaldehyde (CH₂O) solutions (low amount: 0.095 mL, middle amount: 0.19 mL, high amount: 0.38 mL, referred to as Low/Mid/High group in following context) was added, followed by stirring 24 hr. The pTA nanospheres were centrifuged (1736 R; LaboGene, Lillerød, Denmark) at 15,000 rpm (32,310 \times g) for 15 min. The supernatant was removed, and the purified pTA nanospheres were freeze-dried.

2.3. Characterisation

The morphology and elemental analysis of pTA nanospheres were recorded by a field-emission scanning electron microscope (Gemini 500; ZEISS, Oberkochen, Germany). Transmission electron microscopy (TEM) images were taken by TalosTM F200X (FEI; Washington, OR, USA). The samples were first dispersed in ethanol. A drop of the dispersion was supported on a copper grid and then dried prior to TEM characterisation. Fourier-transform infrared (FTIR) spectroscopy (Nicolet iS20 FTIR; Thermo Fisher Scientific, Waltham, MA, USA) was used to confirm the chemical bonding of pTA nanospheres. ¹H-Nuclear magnetic resonance (NMR) spectra were obtained using an Avance Neo 600 MHz-NMR spectrometer (Bruker, Billerica, MA, USA) after dissolving pTA nanospheres in DMSO-d $_{6}$. UV-Vis absorption spectra of pTA nanospheres in DI water were scanned at wavelengths ranging from 200 to 800 nm. The size and zeta potential of pTA nanospheres were measured using a zetasizer (Zetasizer Nano ZS90; Malvern Panalytical, Malvern, UK). The CV diagram was obtained using a VersaSTAT3 (AMETEK; Berwyn, PA, USA). Glassy carbon was used as the working electrode, Ag/AgCl was used as the reference electrode, and a Pt wire electrode was used as the counter electrode. All CV accessories were purchased from Frontier (Seoul, Korea), 0.1 M Tetrabutylammonium hexafluorophosphate and 1.0 mM sample were dissolved in dimethylformamide. The scan rate was 0.1 V s⁻¹. The melting point of pTA nanospheres was measured using an automatic melting point apparatus (SMP50; Stuart, Vernon Hills, IL, USA). The melting point was measured by automatic digital melting point apparatus (Stuart SMP50; Cole-Parmer, Illinois, USA).

2.4. Measurement of total phenolic content

Folin–Ciocalteu reagent was used to determine the total phenolic content [17]. Folin-Ciocalteu reagent ($10 \times$ dilution solution, 2.5 mL) and 1 mL of the sample were mixed and incubated for 5 min under dark conditions. Afterward, 4 mL of 7.5 wt% sodium carbonate solution and 2.5 mL of DI water were added and incubated for 2 hr in a 30° C under dark conditions. After 2 hr of incubation, absorbance was measured at 700 nm. TA was used as a standard for the calibration curve.

2.5. Antioxidant activity assessment

DPPH and ABTS analysis were performed to determine the antioxidant activity of pTA nanospheres [10]. 100 μL of DPPH solution (0.2 mM, in DMSO) was incubated with 100 μL of the sample for 30 min. Absorbance was measured at 517 nm using a microplate reader (Varioskan LUX; Thermo Fisher Scientific, USA). ABTS and 2.45 mmol of

persulfate dissolved in DI water were incubated for 24 h in the dark at room temperature (22 \pm 2°C). The ABTS radical solution was diluted with methanol to achieve 1.10 \pm 0.02 absorption intensity at 732 nm. ABTS (100 $\mu L)$ and the sample (100 $\mu L)$ were then incubated for 30 min to measure the absorbance at 734 nm. Antioxidant activity was calculated as follows:

Antioxidant activity(%) =
$$\frac{A_c - A_s}{A_c} \times 100\%$$

 A_c is the absorbance of the antioxidant tested control (with methanol) solution and A_s is the absorbance of the antioxidant tested sample solution.

2.6. Colony formation assay

MDA-MB-231 (human breast cancer cell line) were seeded at a density of 5×10^4 cells per 500 µL in 24-well plates (Thermo Fisher Scientific, 142475) and maintained in RPMI 1640 medium (Gibco, 11875–119) supplemented with 10 % foetal bovine serum (FBS; Gibco, 16000-44) and 1% antibiotic-antimycotic (AA; 100 x; Gibco, 15240-062). The cells were incubated at 37°C in a humidified 5 % CO₂ atmosphere for 24 h to allow attachment. Following incubation, cells were treated with pTA at an initial concentration of 0.25 mg/mL, followed by a 1:2 serial dilution across seven concentrations, including a control (eight conditions in total, n = 4). After 24 h incubation, cells were fixed with 4 % paraformaldehyde (PFA; Biosesang, PC2031) for 10 min and stained with a 0.5 % crystal violet staining solution prepared by diluting 1 % crystal violet solution (Sigma-Aldrich, V5265) in a 1:1 mixture of distilled H₂O and methanol, for 10 min at room temperature. Images of crystal violet-stained cells were captured using an inverted microscope (ECLIPSE TS100; Nikon, Japan). Quantification was performed using ImageJ software (version 1.54p; NIH, USA). Images were converted to 8-bit greyscale, and a threshold adjustment was applied to measure the total cell-covered area within a 278.94 \times 209.21 μm region for comparative analysis.

2.7. Nucleus count and morphology analysis

MDA-MB-231 cells were seeded at a density of 1×10^4 cells per 100 µL in 96-well plates (Thermo Fisher Scientific, 167008) and incubated for 24 h. Cells were treated with pTA at an initial concentration of 0.25 mg/mL, followed by a 1:2 serial dilution across seven concentrations, including a control (n = 6). After 24 h of pTA treatment, cells were stained with NucBlue™ Live ReadyProbes™ Reagent (Hoechst 33342, Thermo Fisher Scientific, R37605) to visualize nuclei. Fluorescence images were captured at Ex/Em 377/477 nm using a Cytation 1 Imaging system (BioTek, USA) with a 4 × objective. For nuclear morphology analysis, images were processed using ImageJ software with the Extended Particle Analyzer plugin. The analysis workflow included 8-bit conversion, threshold adjustment, binarization, mask conversion, Watershed segmentation, and Extended Particle Analysis. The extracted morphological parameters—area (µm²), perimeter (pixels), Feret's diameter, and roundness—were visualized using violin plots (Origin Pro 8 software, Northampton, MA, USA).

2.8. Focal adhesion analysis by confocal staining

MDA-MB-231 cells were seeded at a density of 5×10^4 cells per 500 μ L per well onto 12-mm cover glass (circular, Marienfeld, 0111520) in a 24-well plate and incubated for adhesion. The medium was then removed, and cells were treated with 0.125 mg/mL pTA for 24 h. Cells were fixed with 4 % PFA for 15 min at room temperature before immunostaining. Fixed cells were permeabilized using 0.5 % TritonTM X-100 (BioXtra, Merck, T9284) in DPBS (Welgene, LB001–02) for 15 min, followed by blocking with 1 % bovine serum albumin (BSA; Bovogen, BSAS1.0) and 0.001 % sodium azide (ReagentPlus®, \geq 99.5 %, Merck,

S2002) in DPBS for 30 min at room temperature to minimize nonspecific binding. For focal adhesion analysis, cells were incubated with anti-Vinculin [SPM227] primary antibody (Ms, Abcam, ab18058) at 1:200 dilution, followed by Donkey anti-Mouse IgG H&L secondary antibody (Alexa Fluor® 555, Abcam, ab150106) at 1:500 dilution. Factin was stained using Actin-Stain 488 Phalloidin (Cytoskeleton Inc., PHDG1), and nuclei were counterstained with Hoechst 33342 (Thermo Fisher Scientific, H3570) at 1:300 dilution. Fluorescence images were captured using a Confocal Laser Scanning Microscope (LSM700; $63 \times oil$ objective; Carl Zeiss, Germany). Dorsal view images were visualized using maximum intensity projection (MIP) in ZEN Microscopy software (blue edition, version 3.3.89.0000; Carl Zeiss, Germany), while 3D reconstructed images were rotated and analysed using IMARIS software (version 9.7.2; Oxford Instruments, United Kingdom). F-actin and vinculin intensity distribution from the nucleus centre to the cell edge was analysed using the line histogram function in ImageJ.

2.9. Intracellular MT1-MMP localisation and actin cytoskeleton analysis

To examine MT1-MMP (MMP14) localisation, cells were incubated with anti-MMP14 [EP1264Y] primary antibody (Rb, Abcam, ab51074, 1:200 dilution), followed by Donkey anti-Rabbit IgG H&L secondary antibody (Alexa Fluor® 555, Abcam, ab150074, 1:500 dilution). F-actin was stained using Actin-Stain 488 Phalloidin and nuclei were counterstained with Hoechst 33342 (Thermo Fisher) at 1:300 dilution. Images were acquired using a Confocal Laser Scanning Microscope (LSM700, $63\times$ oil objective, Carl Zeiss) and analysed using ZEN software for MIP and orthogonal views. Nucleus and F-actin intensity profiles were assessed via line profiling, while ImageJ was used to quantify cell area, F-actin intensity, MMP14 intensity, and colocalization between F-actin and MMP14. The perinuclear distribution of MMP14 was analysed using polar plots and distance-frequency distribution graphs. Fluorescence intensity was measured relative to the nuclear centre, and polar coordinate transformations were applied.

2.10. Cytoskeletal remodelling analysis by high-resolution imaging

Cell preparation was performed under the same conditions as described previously for confocal staining. For immunostaining, cells were incubated with primary antibodies (1:200 dilution), followed by corresponding fluorophore-conjugated secondary antibodies (1:200 dilution) under the following conditions:

- (1) Actin-Stain 488 Phalloidin (Cytoskeleton Inc.,) and anti-Vimentin [D21H3] antibody (XP®, Rb, Cell Signaling Technology, 5741), followed by Goat anti-Rabbit IgG STAR RED (Abberior GmbH, STRED-1002)
- (2) Anti-Vimentin [V9] antibody (Ms, Santa Cruz, sc-6260) and antibeta Tubulin antibody (Rb, Abcam, ab15568), followed by Goat anti-Mouse IgG STAR ORANGE (Abberior, STORANGE-1001) and Goat anti-Rabbit IgG STAR RED (Abberior)
- (3) Anti-beta Tubulin antibody (Abcam) and anti-TOMM20 [4F3] (BSA and Azide-free, Ms, Abcam, ab56783), followed by Goat anti-Rabbit IgG STAR ORANGE (Abberrior, STORANGE-1002) and Goat anti-Mouse IgG STAR RED (Abberior, STRED-1001)

High-resolution imaging was performed using a STEDYCON system (Abberior Instruments GmbH, Germany) in either Confocal or STED mode, depending on the staining conditions. For Confocal mode imaging (condition 1), deconvolution and rendering were conducted using Huygens Professional software (version 24.04; Scientific Volume Imaging B.V., Netherlands). Captured images were processed with Huygens Deconvolution Express, applying the following microscopic parameters: Refractive index (Oil: 1.515), Microscope type (STED), and STED depletion mode (Stedycon). Deconvolution Express Profile was applied, and images were loaded in Twin MIP (Animation) mode for maximum

intensity projection (MIP) rendering. For Confocal and STED mode imaging (conditions 2 and 3), images were acquired directly using the STEDYCON system with STEDYCON Smart Control (browser-based software).

2.11. Gelatine invadopodia assay

To assess invadopodia formation, gelatine-coated coverslips were prepared using the QCM™ Gelatin Invadopodia Assay-Green Kit (Sigma-Aldrich, ECM670), following the manufacturer's protocol. Briefly, coverslips were coated with a thin layer of fluorescein-labelled gelatine, crosslinked with glutaraldehyde, and sterilized with 70 % ethanol before being quenched with growth medium. MDA-MB-231 cells, either untreated or treated with 0.125 mg/mL PTA, were seeded at 1×10^5 cells per 500 µL per well onto gelatine-coated coverslips placed in a 4well cell culture plate (SPL, 3004). After 24 h incubation, cells were fixed with 4 % PFA for 30 min, permeabilized with 0.25 % Triton X-100 in DPBS for 15 min, and blocked with 2 % BSA in DPBS for 30 min. Cells were then stained with TRITC-conjugated phalloidin and DAPI, both included in the ECM670 Kit (Sigma-Aldrich), to visualize F-actin and nuclei, respectively. Invadopodia formation and matrix degradation were assessed by monitoring gelatine degradation areas beneath the cells using a Confocal Laser Scanning Microscope (LSM700; 40 × oil objective; Carl Zeiss). Captured images were processed using IMARIS software (Oxford Instruments) with Surface and MIP mode to generate a dorsal view, and clipping analysis was performed to assess actin invasion into the gelatine degradation regions.

2.12. Real-time cell migration and invasion assay

Cell migration and invasion assays were performed using an xCEL-Ligence Real-Time Cell Analysis (RTCA) DP system (Agilent Technologies, USA) with an RTCA CIM-Plate 16 (Agilent, 56658170001). For the invasion assay, the upper chamber of the CIM-Plate was pre-coated with 20 µL of Matrigel® Basement Membrane Matrix (1:20 dilution, Corning®, 354234) and incubated at 37°C for 4 h. After coating, the bottom chamber was filled with 160 µL of growth medium containing 10 % FBS as a chemoattractant. The upper and bottom chambers were then assembled, and 50 μL of serum-free medium (SFM) was added to the upper chamber, followed by incubation at 37°C for 1 h to equilibrate. After equilibration, background measurement was performed. For cell preparation, MDA-MB-231 cells (1 \times 10⁶ cells per 10 mL) were cultured for 24 h and treated with 0.125 mg/mL PTA. Cells were then harvested and seeded at 4×10^4 cells per 100 µL per well in the upper chamber of the RTCA CIM-Plate in SFM (n = 4 per condition). After seeding, cells were allowed to settle at room temperature for 30 min before mounting the CIM-Plate 16 onto the xCELLigence RTCA DP system. Real-time cell index (CI) measurements were recorded for 48 h to monitor migration and invasion dynamics.

2.13. Metabolic analysis

Metabolic measurements were performed using a Seahorse XFe24 Analyzer (Agilent Technologies, USA) with the Mito Stress Test (Agilent, 103015) and Real-Time ATP Rate Assay (Agilent, 103592) Kit, following the manufacturer's protocols. MDA-MB-231 cells were seeded in XF24 Cell Culture V7-PS Microplates (TC-treated, Agilent, 100777) at a density of 2.5×10^4 cells per 250 μL per well (n = 3) and incubated for adhesion. Cells were treated with 0.125 mg/mL PTA for 24 h before metabolic analysis. For the Real-Time ATP Rate Assay, cells were sequentially treated with 2 μM oligomycin and 0.5 μM rotenone/antimycin A (Rot/AA). For the Mito Stress Test, cells were sequentially treated with 2 μM oligomycin, 0.5 μM FCCP, and 0.5 μM Rot/AA. Hoechst 33342 (Thermo Fisher Scientific, H3570) staining was performed at the end of the assay for normalization, with results normalized to 8000 and 10000 units, respectively. Metabolic data were analysed

using Wave software (version 2.6.1.53, Agilent) to quantify assay results.

2.14. Reactive oxygen species (ROS) measurement

Intracellular ROS levels were assessed using the DCFDA/H2DCFDA Cellular ROS Assay Kit (Abcam, ab113851). Stock solutions were prepared as follows: tert-Butyl hydroperoxide (TBHP; 55 mM stock) was diluted to 1000 μM and then to a final concentration of 100 μM for the positive control; DCFDA (20 mM in DMSO) was diluted to 200 μ M and further to 20 µM for cell staining. MDA-MB-231 cells were seeded at a density of 1×10^4 cells per 100 µL per well in a 96-well black plate (Corning, 3603) and incubated for adhesion. The medium was then removed, and cells were treated with 0.125 mg/mL PTA. After 20 h of incubation, the medium was removed, and 100 µL per well of 1x assay buffer was added. For the positive control, TBHP was added and incubated for 4 h. The buffer was then removed, and cells were stained with the diluted DCFDA solution. Cells were incubated with DCFDA solution for 45 min at 37°C in the dark, followed by two washes with 1x buffer before live-cell imaging. Fluorescence was captured using a Cytation 1 imaging system (BioTek) with a 20 × objective at Ex/Em 469/525 nm, and mean fluorescence intensity was quantified for each condition (n = 4).

2.15. Transmission electron microscopy (TEM) imaging

MDA-MB-231 cells (1 \times 10⁶ cells per 10 mL) were cultured for 24 h and treated with 0.125 mg/mL PTA for 24 h. For TEM sample preparation, cells were harvested (1 × 106 cells per sample), centrifuged at $250-300 \times g$ for 3 min, and the supernatant was removed. Cells were fixed in 2 % glutaral dehyde (Fisher Chemical, O2957–1) and 2 % PFA (Merck, 818715) in 0.1 M phosphate buffer (pH 7.4, Sigma, S7907 [dibasic], S9638 [monobasic]) for 12 h, post-fixed in 1 % osmium tetroxide (OsO4; Polysciences, 0223) for 2 h, and dehydrated using a graded ethanol series. Samples were embedded in Poly/Bed 812 resin (Polysciences, 08792-1) and polymerized at 70°C for 12 h. Ultrathin sections (approximately 80 nm) were obtained using an Ultramicrotome (UC7; Leica Microsystems, Germany) with a diamond knife, placed on copper grids, and double-stained with 5 % uranyl acetate (20 min; EMS, 22400) and 3 % lead citrate (7 min; Leica, 16707235). TEM imaging was performed using an HT7800 electron microscope (Hitachi, Japan) at 100 kV with an RC camera at 42,000 \times magnification (\times 42 K).

2.16. Glutathione (GSH/GSSG) ratio measurement

The intracellular glutathione ratio was quantified using the GSH/ GSSG Ratio Detection Assay Kit II (Fluorometric-Green; Abcam, ab205811) according to the manufacturer's protocol. MDA-MB-231 cells were seeded at a density of 1×10^6 cells per 10 mL in 100 mm culture dishes and incubated for 24 h before treatment with 0.125 mg/ mL PTA. After 24 h of treatment, cells were collected and resuspended in $300\,\mu L$ of ice-cold 1x RIPA buffer (3 \times 10^6 cells per sample; Cell Signaling, 9806S). The lysates were homogenized by pipetting up and down, followed by centrifugation at 13,000 rpm (15,871 \times g) for 15 min at 4°C (Eppendorf, Germany, 5425 R) to remove insoluble debris. For sample preparation, deproteinization was performed using the Deproteinizing Sample Kit-TCA (Abcam, ab204708), followed by protein precipitation and sample neutralization. The final protein concentration was adjusted to 2×10^4 cells per 50 μL of 1x RIPA buffer per well. Each well was treated with either the GSH assay mixture or the total glutathione assay mixture and incubated while fluorescence was monitored every 10 min using a Cytation 1 imaging system (BioTek). GSH quantification was conducted using a standard curve method. A calibration curve (0–10 $\mu M)$ was generated in duplicate, and fluorescence intensity (RFU) was recorded at Ex/Em 490/520 nm. The standard curve exhibited high linearity ($R^2 = 0.99$), ensuring accurate quantification.

Sample RFU values were mapped to the standard curve to determine intracellular GSH concentrations. Total glutathione levels (GSH \pm GSSG) were measured, and oxidized glutathione disulfide (GSSG) was calculated using the following formula:

$$GSSG = \frac{Total\ Glutathione - GSH}{2}$$

The GSH/GSSG ratio was determined to assess oxidative stress levels.

2.17. Western blot analysis

Total protein was extracted from untreated or 0.125 mg/mL PTA-treated MDA-MB-231 cells using 1x RIPA buffer (10x, Cell Signaling, 9806S) supplemented with 1 mM PMSF (200 mM; Cell Signaling, 8553) and 1x Protease/Phosphatase Inhibitor Cocktail (100x; Cell Signaling, 5872S). Protein concentration was determined using the Pierce™ BCA Protein Assay Kit (Thermo Fisher Scientific, 23227) at 562 nm, following the manufacturer's instructions. Samples were separated on 8–12 % SDS-PAGE gels (Biosesang, SR2003–050–00; SF2002–110–00) and transferred to Immobilon-P PVDF membranes (Millipore, IPVH00010) using standard techniques. Membranes were blocked with 5 % Non-Fat Powdered Milk (Biosesang, N1059) or BSA (Bovogen) in 1x TBS (w/Tween-20) (10x, Biosesang, TR2006–100–00) and incubated with primary antibodies overnight at 4°C, followed by HRP-conjugated secondary antibodies (1:2000 dilution; Cell Signaling, 7074S or 7076S) for 2 h at room temperature.

Western blotting was conducted to evaluate protein expression profiles under various treatment conditions. Cell lysates were separated by SDS-PAGE using 8–12 % gels, followed by transfer onto PVDF membranes. Protein loading amounts, gel compositions, electrophoresis and transfer parameters, as well as blocking conditions and antibody dilutions, were selected according to the molecular weights of target proteins and optimized for each antibody. Detailed experimental conditions, including antibody sources and blocking reagents, are summarized in **Table S1**. Protein bands were detected using Immobilon Western Chemiluminescent HRP Substrate (Millipore, WBKLS0500), and signals were visualized with AmershamTM ImageQuantTM 800 (Cytiva, USA). Densitometric analysis was performed using ImageQuantTM TL analysis software (version 10.2, Cytiva).

2.18. Statistical analysis

All quantitative data were obtained from parallel experiments with at least three independent replicates (n \geq 3), and are expressed as mean \pm standard deviation (SD). Statistical comparisons between two groups were performed using Student's *t*-test. In addition, statistical analysis was performed where appropriate, and significant differences have been marked in the figures using standard asterisk notation (*p < 0.01, **p < 0.05).

3. Results and discussion

3.1. Preparation and characterisation of nanospherical poly(tannic acid)

Tannic acid (TA) molecules were crosslinked to form pTA nanospheres using a modified Stöber method, which was inspired by the synthesis of resorcinol–formaldehyde resin spheres [18,19]. The oxygen and hydrogen atoms of F-127 formed hydrogen bonds with hydroxyl groups of TA. Since F-127 formed nano-assemblies in aqueous phase, TA trapped on the surface of the F-127 cooperated nanosphere [20], allowing TA to be polymerized by formaldehyde (CH₂O) to produce pTA nanospheres (Fig. 1b). The hydrodynamic diameter (black bars) and zeta potential (red line) of pTA nanospheres synthesized using different concentrations of formaldehyde: Low (L), Medium (M), and High (H) were measured. The particle size significantly decreased with increasing formaldehyde concentration, indicating enhanced crosslinking density

and the formation of a more compact nanostructure (Fig. S1). The zeta potential also became more negative with higher formaldehyde levels, reflecting increased colloidal stability due to the higher surface charge. This trend suggests that formaldehyde concentration plays a key role in modulating both the physical and surface properties of pTA nanospheres. Scanning electron microscopy (SEM) images revealed that the shape and distribution of pTA depended on the formaldehyde concentration (Fig. 1c). At high formaldehyde concentrations, the synthesized pTA exhibited a uniform spherical morphology with an average diameter of $110.5 \pm 12 \text{ nm}$ (n ≥ 100 ; More than 100 individual particles were counted and measured particle size across multiple image regions to ensure statistical reliability). In contrast, at low and medium concentrations of formaldehyde, the pTA particles were irregular in shape and agglomerated. Formaldehyde concentration appears to be a critical parameter for the preparation of pTA nanospheres. To determine the optimal synthetic time for formation of pTA nanosphere, we additionally observed morphology and particle size at different reaction time points (0, 0.5, 1, 2, 4, and 24 h) by SEM image and light scattering analysis, respectively. As shown in Fig. S2, we observed that particle formation initiated after 1 h – the particles were heterogeneous in size and shape. Among the reaction time points, after 24 h, we obtained uniform spherical nanostructures with an average diameter of ~100 nm. Additionally, TEM analysis confirmed that the particles were non-porous and maintained a spherical structure (Fig. S3).

To confirm the polymerization and structural modifications of TA during the pTA formation, FT-IR and ¹H NMR spectroscopy were conducted. The FT-IR spectrum confirmed the characteristic functional groups of TA and its polymerized form in pTA (Fig. 1d and Fig. S4). The O-H stretching vibration was observed in the range of 3350–3280 cm⁻¹, while the benzene ring (C=C) vibration appeared at 1589 cm⁻¹, indicating the preserved aromatic structure of TA [21,22]. For F-127, the characteristic -CH stretching was observed at 2870 cm⁻¹ [20], while the formaldehyde-derived -CH stretching appeared at 2900 cm⁻¹ (Fig. S5) [21]. These findings confirm that TA molecules were successfully adsorbed onto the F-127 nanoassemblies and polymerised via formaldehyde crosslinking. The ¹H NMR spectrum further validated the structural transformation of TA into pTA (Fig. 1e). A downfield shift of the CH₂ proton signal from $\delta = 9.5$ to $\delta = 4.3$ was observed, indicating the successful incorporation of methylene (-CH2) linkages through formaldehyde-mediated polymerization [23,24]. The broad O-H proton signals were detected in the range of $\delta = 9.4-9.2$, while the aromatic proton signals appeared at $\delta = 7.1$ –6.9, confirming the retention of the benzene ring structure [25]. These spectral changes confirm that formaldehyde facilitated the polymerization of TA by reacting with its phenol groups, leading to the formation of a stable pTA nanospherical structure.

The thermal properties of pTA were assessed using an automatic digital melting point apparatus (Fig. 1f). The measured melting points of TA (218°C) and F-127 (56.8°C) were consistent with previously reported values, confirming the reliability of the measurements [26,27]. In contrast, pTA showed a melting point exceeding 300° C, indicating a substantial enhancement in thermal stability compared to TA [25,28]. This increase in melting temperature suggests that polymerization led to a more thermally robust structure, likely due to increased intermolecular interactions and crosslinking within the pTA network.

3.2. Amplified antioxidant activity of pTA nanospheres

To quantify the amount of TA incorporated within the pTA nanospheres, a Total Phenol Content (TPC) assay was performed (Fig. S6). The TPC assay is a widely used analytical method for determining the concentration of phenolic compounds in a sample, based on their ability to reduce the Folin–Ciocalteu reagent and produce a colorimetric response measurable by spectrophotometry. The assay results indicated that at a pTA 0.5, 0.25 and 0.125 mg/mL, the detected TA content were 0.33717, 0.19191 and 0.09701 mg/mL. Based on these measurements, it was determined that 73.94 ± 4.6 % of the pTA composition consists of

TA, confirming the successful incorporation of TA into the polymerized spherical nanostructure. UV-Vis spectrophotometry confirmed the characteristic absorption peak of TA at 275 nm, which remained unchanged in pTA, indicating the retention of antioxidant properties (Fig. 1g) [29]. Cyclic voltammetry (CV) analysis further revealed that pTA exhibited an irreversible oxidation peak with a lower oxidation potential, suggesting enhanced oxidation stability and resistance (Fig. 1h and Fig. S7) [10,30]. To investigate the origin of the antioxidant activity of pTA nanosphere, antioxidant activity of reactants (TA, F-127, ammonia, formaldehyde) was evaluated, indicating that the activity of pTA nanosphere was originated from assembly of TA (Fig. 1i). Quantitative antioxidant assays demonstrated that pTA achieved an antioxidant efficiency of approximately 90 % at a concentration of 0.031 mg/mL, indicating superior radical-scavenging capability (Fig. 1j) [21]. Solubility tests revealed that pTA remained dispersed as a structured assembly in ethanol, while it dissolved in DMSO (Fig. S8). In Fig. 1k, antioxidant activity measurements in DMSO showed higher antioxidant efficacy, likely due to the exposure of inner TA molecules upon dissolution, further enhancing radical scavenging ability. These findings collectively suggest that pTA not only retains but significantly enhances the antioxidant capacity of TA, thereby enhancing its potential efficacy in cancer metastasis suppression.

Based on theoretical calculation using chemical structure, 11,824 molecules of TA would construct to single pTA nanosphere. We assumed that area of a TA molecule would be 2.66 nm² (length of TA: 1.63 nm) and area of a pTA nanosphere would be 31,416 nm² (diameter of a pTA sphere: 100 nm). Since the amplified antioxidant activity is included in single pTA sphere, it is referred to as a nano-antioxidant in the following studies.

3.3. Antioxidative impact of pTA nanospheres cellular proliferation and nucleus morphology

To investigate the nuclear-level effects of pTA nanospheres on triple-negative breast cancer (TNBC) cells, MDA-MB-231 cells were treated with increasing concentrations of pTA (0.004–0.250 mg/mL) for 24 h (Fig. 2a). A gradual fading of crystal violet staining was observed with higher pTA concentrations, indicating a decrease in cell viability; this trend was more clearly visible under higher magnification in brightfield microscopy (Fig. 2b). Quantification of the total cell-covered area confirmed that cellular proliferation was significantly suppressed in a dose-dependent manner following pTA nanospheres treatment (Fig. 2c).

High-content fluorescence imaging of Hoechst-stained nuclei revealed a marked reduction in nuclear count at concentrations $\geq 0.125~\text{mg/mL},$ suggesting that pTA nanospheres exert strong antiproliferative effects, likely through inhibition of cell cycle progression or induction of a quiescent state (Figs. 2d and 2e) [31]. Furthermore, quantitative morphometric analysis of individual nuclei demonstrated that, while nuclear area and perimeter remained relatively stable, nuclear roundness progressively increased with higher pTA nanosphere doses, indicating a shift toward more spherical nuclear morphology (Fig. 2f). This may reflect cytoskeletal relaxation or chromatin condensation in response to redox-mediated stress signalling [32,33].

This shift toward more isotropic nuclear morphology—with roundness values approaching 1.0 at higher doses—indicates a loss of nuclear elongation and polarity, independent of overall size reduction. The subtle decrease in the Feret diameter and perimeter further supports this interpretation, implying that pTA nanospheres-treated nuclei undergo geometric simplification rather than compaction. These changes suggest a mechanically relaxed nuclear state, characterized by reduced nuclear deformation, potentially due to alterations in the mechanical forces transmitted to the nucleus or chromatin remodelling events [34]. Thus, these observations demonstrate that pTA nanospheres not only reduce TNBC cell proliferation but also reshape nuclear morphology toward a more spherical, less polarized architecture, consistent with suppressed mechanical signalling and reduced nuclear plasticity.

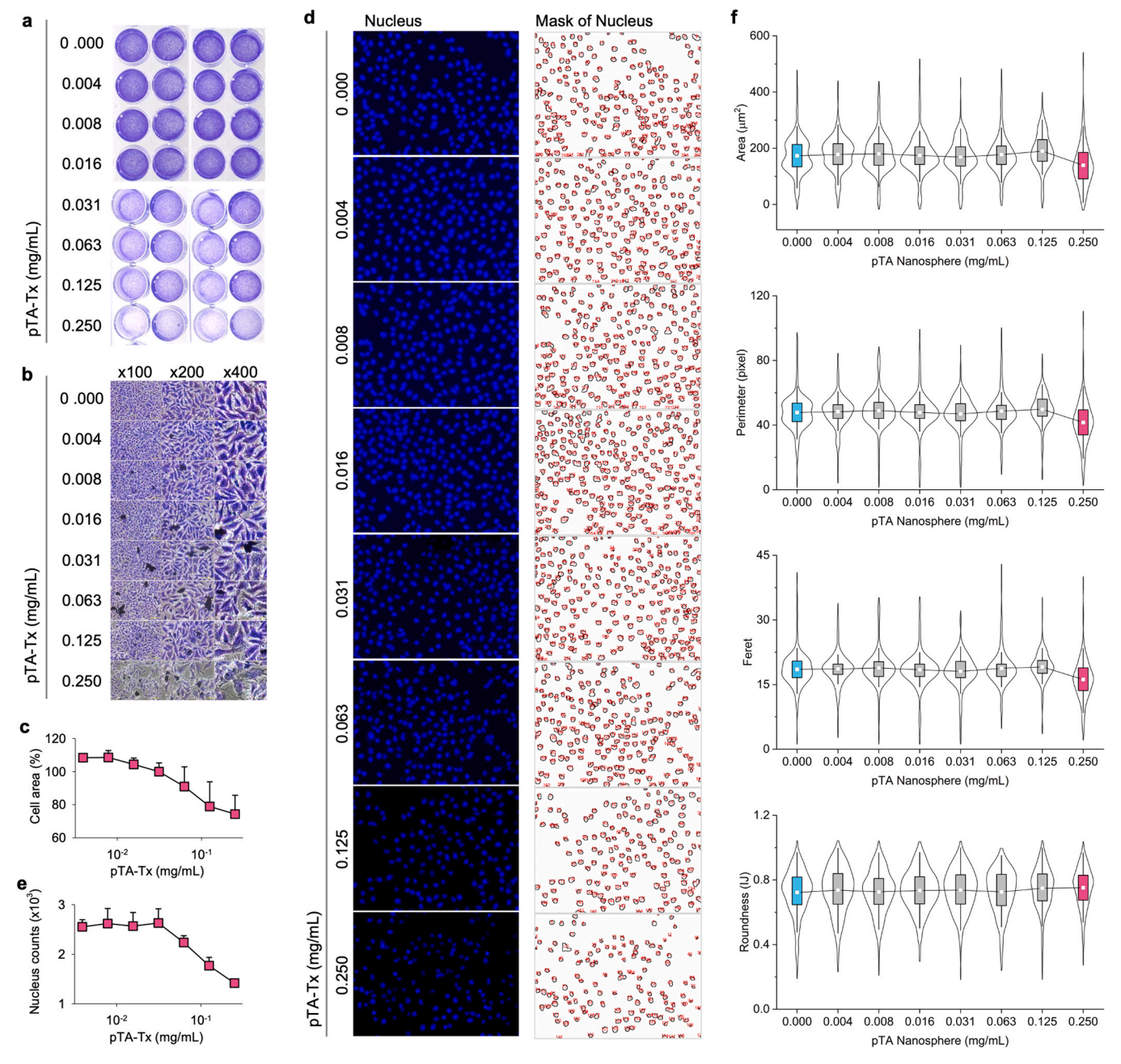


Fig. 2. Dose-dependent effects of pTA nanospheres on MDA-MB-231 cell viability and nuclear morphology. a Crystal violet staining of MDA-MB-231 cells treated with increasing concentrations of poly(tannic acid) (pTA) nanospheres for 24 h. b Brightfield microscopy of CV-stained cells at magnifications of $100 \times$, $200 \times$, and $400 \times$. c Quantification of total cell-covered area (%) relative to untreated control. d Quantification of nuclear count (%) via high-content imaging, normalized to control. e High-content fluorescence images of nuclei (Hoechst, blue) and corresponding binary nuclear masks across treatment conditions. f Violin plots of nuclear morphological parameters (area, perimeter, Feret diameter, and roundness), measured from segmented nuclei under the 0.125 mg/mL pTA treatment condition.

3.4. Disruption of cytoskeletal architecture and focal adhesion dynamics by pTA treatment

Treatment with pTA nanospheres induced remarkable changes in the cytoskeletal organisation and mechanical phenotype of MDA-MB-231 cells (Fig. 3a). Dual immunofluorescence staining for F-actin and vinculin was performed not only to observe overall cell morphology but also to precisely evaluate focal adhesion structures and lamellipodia dynamics [35,36]. In non-treated control cells, actin filaments were well-organized, forming prominent stress fibres that aligned with elongated cell shapes, while vinculin localized strongly at defined focal adhesions near the cell periphery—features consistent with mechanically active and polarized cells exhibiting robust lamellipodial activity

(Figs. 3b and 3c).

After the treatment with pTA nanospheres, cytoskeletal architecture was markedly disrupted. Cells exhibited a more isotropic and flattened morphology, accompanied by disassembled actin networks and a notable reduction in cortical F-actin (Fig. 3d). Vinculin staining became more diffuse, with loss of punctate localisation, indicating focal adhesion disassembly. Z-stack reconstruction and intensity line profiling further confirmed the loss of polarized actin structures and diminished actin accumulation near the basal membrane (Fig. 3e). To further visualize the spatial distribution of cytoskeletal and adhesion components, line scans were drawn radially from the nuclear centre to the cell periphery across multiple directions in both control and pTA-treated MDA-MB-231 cells [37]. These line profiles were used to generate

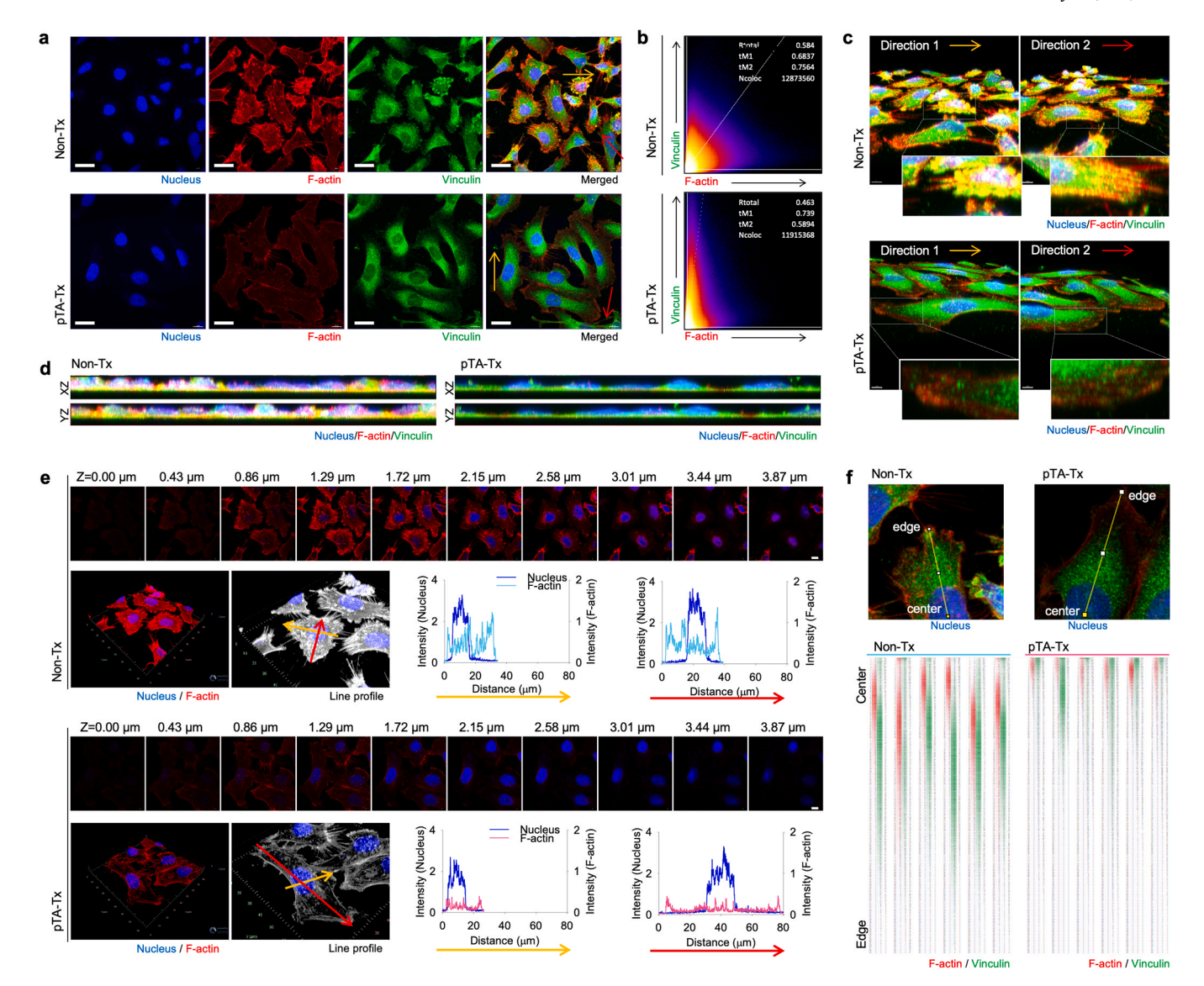


Fig. 3. Cytoskeletal and focal adhesion remodelling upon pTA nanosphere treatment in TNBC cells. a Immunofluorescence staining of MDA-MB-231 cells revealing nuclei (blue), F-actin (red), and vinculin (green) in control and pTA-treated groups, visualized from the dorsal view (XY plane). Merged images highlight disruption of actin stress fibres and focal adhesion organisation following pTA treatment. Arrows indicate representative focal adhesions at the cell periphery. b Colocalization analysis between F-actin and vinculin using scatter plots (Pearson's correlation). The pTA group shows reduced Rtotal and tM2 values, indicating diminished actin-vinculin coupling. c 3D surface reconstruction images in two rotational directions. Control cells display distinct actin-vinculin structures along the basal surface, whereas pTA-treated cells show reduced and scattered cytoskeletal features. Insets show magnified basal plane areas. d Orthogonal (XZ/YZ plane) projections across the z-axis. Control cells exhibit vertically layered actin-vinculin-nuclear architecture, while pTA-treated cells appear flattened with disrupted vertical actin organisation. e Confocal z-stack images and 3D reconstructions of nuclei (blue) and F-actin (red). Line profile analysis along orthogonal vectors (yellow, red) quantifies F-actin and nuclear intensity. PTA treatment reduces actin intensity and disorganizes perinuclear actin structure. f Line scan and heatmap visualization of F-actin and vinculin distribution from nuclear centre to cell edge. Control cells show periodic alignment of actin and vinculin, whereas pTA-treated cells display blurred, irregular signal patterns, indicating cytoskeletal disarray and focal adhesion impairment.

radial intensity heatmaps depicting the localisation of F-actin (red) and vinculin (green) signals (Fig. 3f). In control cells, F-actin and vinculin intensities were strongly polarized toward the leading edge, consistent with active lamellipodia formation and focal adhesion engagement. In contrast, pTA-treated cells showed markedly diminished signal intensities and spatial restriction of both markers near the nuclear region, with limited extension toward the periphery. This suggests a loss of mechanical polarity and suppression of edge-directed cytoskeletal remodelling and adhesion dynamics, indicative of mechanically quiescent and migration-incompetent phenotypes following pTA exposure [36,38,39]. These data collectively illustrate that pTA treatment not only alters cell shape but imposes a profound shift in cytoskeletal mechanics, impairing the physical structures necessary for motility and

invasion. The mechanical phenotype transition from elongated, polarized, and contractile cells to flattened, rounded, and tension-deficient ones underscores the mechanoregulatory effect of pTA in functionally suppressing TNBC invasiveness via disruption of the F-actin–vinculin axis.

3.5. Spatial reprogramming of MT1-MMP under antioxidant stress

To investigate how pTA nanospheres influence MT1-MMP distribution in triple-negative breast cancer (TNBC) cells, we performed multichannel confocal imaging and quantitative spatial analysis in MDA-MB-231 cells under control and pTA-treated conditions. MT1-MMP (membrane type 1 matrix metalloproteinase) is a membrane-anchored

protease that plays a pivotal role in cancer cell invasion by enabling pericellular degradation of the extracellular matrix (ECM), particularly at the leading edge of migrating cells and within invadopodia structures [40–42]. Its polarized localisation and trafficking to actin-rich protrusions are tightly regulated and redox-sensitive, making it a critical effector in metastasis [43–45]. In dorsal-view XY plane microscopic images (Fig. 4a), MT1-MMP was preferentially localized along F-actin-enriched protrusions in control cells, consistent with its known role in focalized matrix degradation at invasive fronts. However, after the treatment with pTA, MT1-MMP was redistributed away from the periphery and accumulated more diffusely near the perinuclear region.

This shift was supported by colocalization analysis, where Pearson's and Manders' coefficients (Fig. 4b) indicated reduced overlap between F-actin and MT1-MMP in pTA-treated cells, suggesting disruption of protease targeting to actin-based structures. Vertical 3D reconstructions (Fig. 4c) and orthogonal XZ/YZ projections (Fig. 4d) further highlighted a loss of MT1-MMP enrichment at the cortical zone, with fluorescence signals repositioned deeper into the cytosol in the treated group. Quantitative image analysis revealed that although total MT1-MMP intensity was modestly reduced, a substantial portion of the protease was redistributed away from the cell edge (Fig. 4e). Concomitantly, peripheral F-actin intensity was diminished (Fig. 4f), indicating that cytoskeletal disassembly may underlie the impaired delivery of MT1-MMP to invasive membrane domains. Single-cell images and corresponding angular polar plots (Fig. 4g-h and Fig. S9) clearly demonstrated a loss of MT1-MMP polarization toward a singular leading edge, reinforcing the notion of disrupted directional invasion.

Further compartmental intensity analysis (Fig. 4i) confirmed an increased proportion of MT1-MMP localized to the nuclear vicinity, and distance-frequency plots (Fig. 4j) quantitatively validated this perinuclear confinement. These spatial shifts are likely driven by the antioxidant properties of pTA, which reduce intracellular ROS and disrupt ROS-sensitive cytoskeletal and vesicular trafficking networks. Given that MT1-MMP's functional positioning at the invasive front is essential for invadopodia maturation and ECM remodelling, the observed mislocalisation under pTA treatment provides a compelling mechanistic explanation for reduced invasiveness. By disrupting redox-regulated trafficking of MT1-MMP, pTA nanospheres effectively suppress a critical step in metastatic dissemination [10]. Collectively, these findings demonstrate that pTA nanospheres exert spatial and functional repression of MT1-MMP in TNBC cells, leading to impaired matrix degradation and invasion. This highlights the therapeutic promise of redox-targeted nanomaterials for the effective suppression of metastatic behaviour in aggressive breast cancers.

3.6. Antioxidant pTA disrupts cytoskeletal coordination and ECM remodelling

pTA nanospheres significantly impaired the invasive behaviour of MDA-MB-231 cells, which can be attributed to their potent antioxidant effects that disrupt redox-sensitive cellular processes. In the 3D gelatine degradation assay (Fig. 5a), control cells displayed prominent invadopodia-like structures and local gelatine degradation, indicative of active ECM remodelling. In contrast, pTA-treated cells exhibited markedly reduced F-actin-enriched protrusions and minimal ECM degradation, suggesting a suppression of matrix-degrading activity. This inhibition of matrix degradation was accompanied by decreased invasion capacity, as shown in the real-time xCELLigence assays. While both migration (Fig. 5b) and invasion (Fig. 5c) were suppressed upon pTA exposure, the inhibitory effect was more pronounced in the invasion assay. Migration exhibited a moderate decline in cell index over time, whereas invasion through gel-coated membranes exhibited a substantial reduction, suggesting that pTA dampens not only motility but also matrix remodelling capacity. These results reveal a redox-driven disruption of both locomotion and proteolytic invasion machinery.

Mechanistically, confocal microscopic imaging of the cytoskeleton

revealed profound structural changes following pTA treatment. Vimentin, a redox-sensitive intermediate filament protein known to regulate epithelial-mesenchymal transition (EMT), invasive protrusions, and cellular elasticity, appeared more compact and disorganized in treated cells, with a loss of polarized filament alignment (Fig. 5d) [46,47]. In the context of cancer progression, vimentin promotes cytoskeletal adaptability and supports the formation of stable invadopodia by scaffolding actin networks and facilitating focal adhesion maturation. Specifically, in the control condition, vimentin filaments were densely aligned around the nucleus and extended directionally toward the cell periphery, forming a scaffold that likely supports nuclear positioning and directional migration. In contrast, pTA-treated cells exhibited diffuse vimentin distribution, failing to envelop the nucleus effectively and instead spreading throughout the cytoplasm without orientation. This aberrant pattern implies a breakdown of the structural polarity necessary for efficient cell migration and matrix invasion. Moreover, super-resolution imaging using STED microscopy provided critical insight into the co-disruption of vimentin and β-tubulin networks following pTA treatment (Fig. 5e and Fig. S10) [48]. β-tubulin, a key component of microtubules, plays a pivotal role in maintaining intracellular polarity and directing vesicular trafficking toward the cell front during migration and invasion [49]. Together with vimentin, which provides structural support and mediates cytoskeletal plasticity, these filament systems cooperate to form a coordinated intracellular scaffold that facilitates the targeted transport of matrix-degrading proteases such as MT1-MMP [46]. While conventional confocal microscopy (Fig. 5d) revealed broader cytoskeletal reorganisation, STED microscopy allowed nanoscale resolution of filament architecture, enabling visualization of subtle disorganisation and uncoupling between vimentin and β-tubulin that are not readily captured by diffraction-limited techniques. Under pTA-induced antioxidant stress, this loss of filament integrity and spatial coordination likely impairs the directed transport of proteolytic vesicles to the invasive front, thereby limiting ECM degradation and metastatic progression. The use of STED imaging was critical for identifying these fine-scale alterations in filament continuity and alignment, supporting the conclusion that antioxidant modulation by pTA disrupts key structural pathways required for invasive migration. Altogether, these findings indicate that pTA nanospheres modulate cancer cell invasiveness through their antioxidant activity by suppressing ROS-dependent cytoskeletal dynamics, vimentin-mediated structural polarization, vesicle trafficking, and ECM degradation, without inducing overt cytotoxicity. This reinforces the potential of redox-targeted nanotherapeutics for the non-lethal control of metastatic behaviour in aggressive cancers.

$3.7.\$ Redox-driven mitochondrial remodelling and metabolic reprogramming by pTA nanospheres

To investigate the functional impact of pTA nanospheres on triplenegative breast cancer (TNBC) cells, a comprehensive multiparametric analysis was conducted to assess metabolic output, redox balance, and cytoskeletal remodelling in MDA-MB-231 cells. The Mito Stress Assay revealed a significant decline in basal oxygen consumption rate (OCR), dropping from approximately 50 pmol/min/10,000 cells in control cells to 32 pmol/min/10,000 cells following pTA treatment (Fig. 6a, left). Similarly, maximal respiration was reduced by nearly 50 %, reflecting a loss in mitochondrial reserve capacity. The extracellular acidification rate (ECAR), indicative of glycolytic activity, decreased from 9 to 8 mpH/min/10,000 cells under pTA treatment (Fig. 6a, right). These changes were collectively illustrated in the OCR vs. ECAR scatter plot (Fig. 6b), depicting a clear transition from an energetically active state to a metabolically quiescent phenotype. The OCR linked to ATP production also declined, halving from approximately 12 to 7 pmol/min (Fig. 6c). Further, the ATP Rate Assay demonstrated reduced ATP synthesis from both glycolytic and mitochondrial sources (Fig. 6d). Specifically, mitochondrial ATP production was remarkably reduced, from

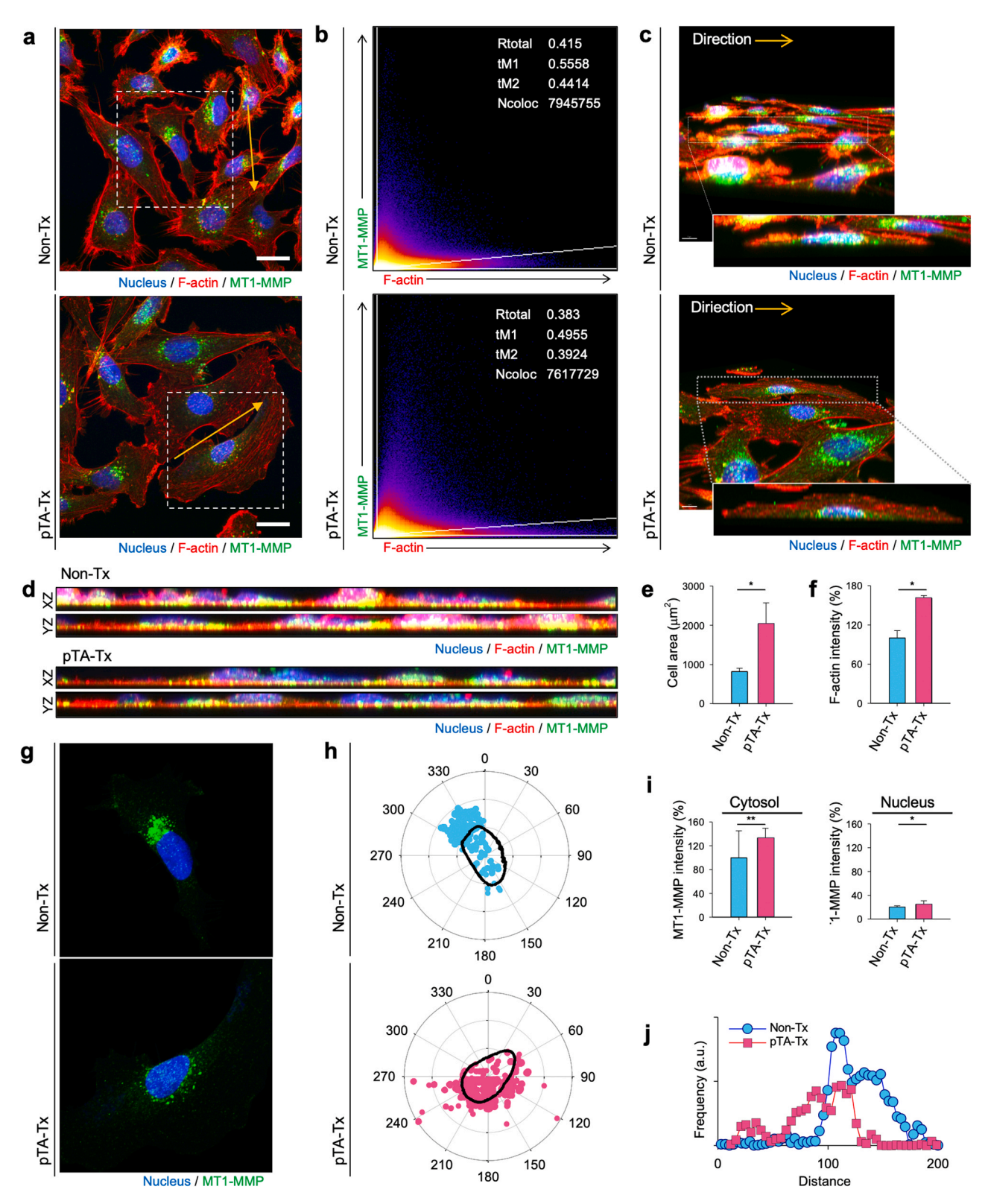


Fig. 4. pTA nanospheres induce redistribution and perinuclear confinement of MT1-MMP in TNBC cells. a Immunofluorescence images of MDA-MB-231 cells depicting F-actin (red), MT1-MMP (green), and nuclei (blue) in non-treated control and pTA-treated conditions, captured from the dorsal view (XY plane). Scale bars mean 20 μ m. b Scatter plots depicting the colocalization between F-actin and MT1-MMP, quantified using Pearson's R and Manders' coefficients. c 3D confocal reconstructions (indicated direction from a) illustrating vertical distribution of MT1-MMP relative to actin-rich structures. d Orthogonal (XZ/YZ plane) projections highlighting cortical versus intracellular MT1-MMP localisation. e Quantification of cell area and total MT1-MMP intensity (*p < 0.01). f Quantification graph for F-actin intensity (*p < 0.001). g Single-cell images showing the relative polarization of MT1-MMP with respect to the nucleus. h Polar plots quantifying angular MT1-MMP distribution around the nucleus. i Quantification of MT1-MMP intensity in cytosolic and nuclear regions (*p < 0.01), **p < 0.05). j Distance-frequency histograms of MT1-MMP localisation from the nuclear centroid.

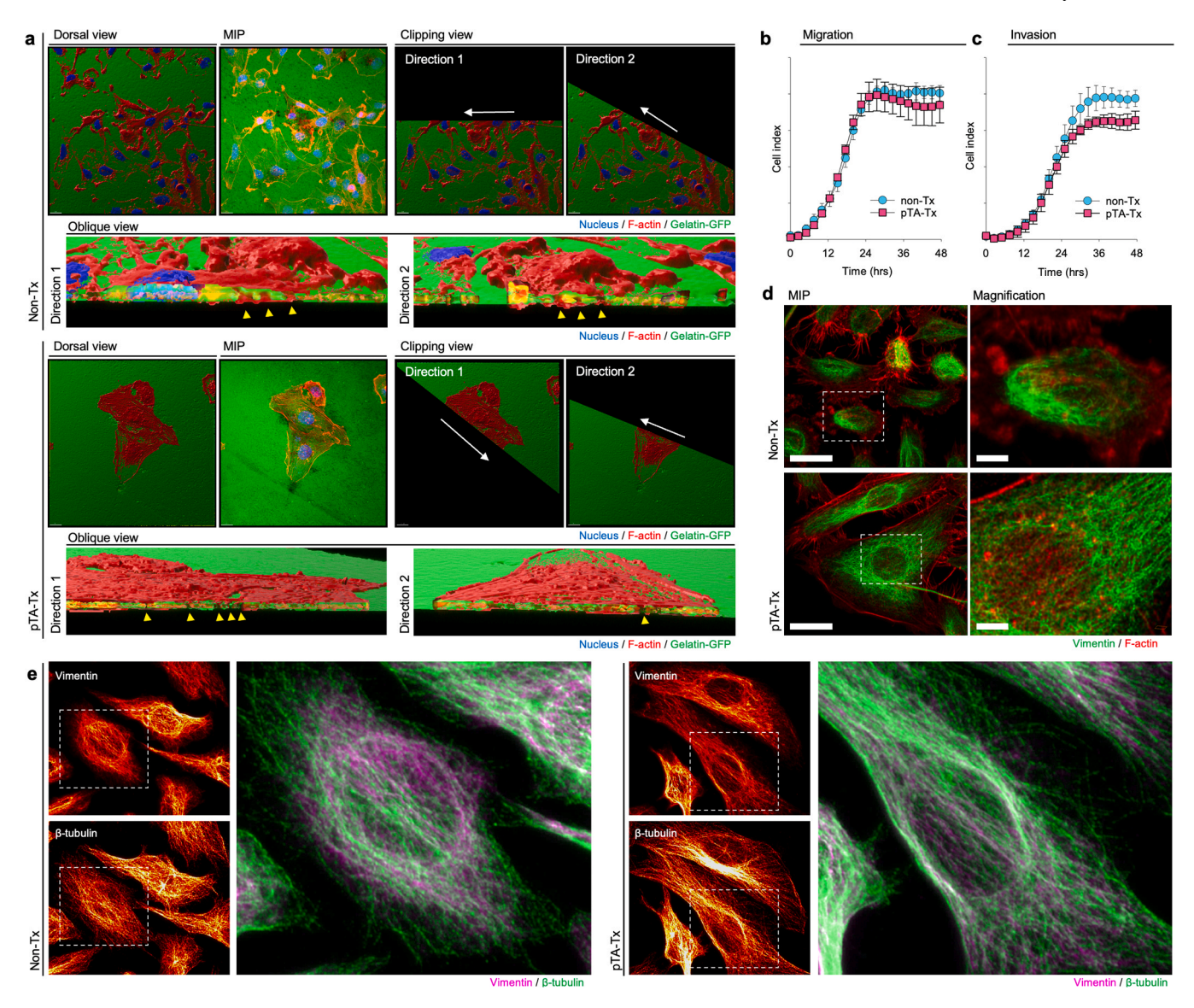


Fig. 5. pTA nanospheres suppress ECM degradation and invasion in cancer cells. a 3D confocal reconstruction of gelatine degradation assay showing nucleus (blue), F-actin (red), and gelatine-GFP (green); includes dorsal view, maximal intensity projection, clipping, and lateral views. Real-time cell b migration and c invasion assay comparing control and pTA-treated MDA-MB-231 cells. d Maximum intensity projection (MIP) and magnified confocal microscopic images of cells stained for vimentin (green) and F-actin (red) under control and pTA nanosphere-treated conditions. Left panels show whole-cell views; right panels present zoomed-in regions marked by dashed boxes. Scale bars: 20 μm (left), 5 μm (right). e Super-resolution microscopic images of vimentin (STAR Orange) and β-tubulin (STAR Red) in control and pTA-treated cells.

46 to 9 pmol/min (Fig. 6e and Fig. S11). In addition, the contribution of oxidative phosphorylation (OXPHOS) to ATP production was markedly reduced (Fig. 6f), with the XF ATP Rate Index decreasing approximately fivefold, from 0.55 in control cells to 0.11 following pTA treatment (Fig. S12). These metabolic perturbations were paralleled by a critical decline in intracellular reactive oxygen species (ROS) (Fig. S13). Following pTA nanosphere treatment, intracellular glutathione redox profiling revealed a coordinated reduction in both reduced (GSH) and oxidized (GSSG) glutathione levels (Fig. 6g). Total glutathione content was also diminished, indicating a global suppression of glutathionedependent antioxidant turnover. Although the GSH to GSSG ratio slightly decreased (Fig. 6h), the overall balance remained relatively stable, suggesting that cells were not under acute oxidative stress but rather in a redox-quiescent state. This pattern reflects the effect of pTA as a potent ROS scavenger, which likely lowered intracellular ROS burden to the extent that endogenous glutathione utilization was reduced. The mild decrease in GSH to GSSG ratio further implies a modest shift toward a more oxidized environment, yet still within the

range of cellular redox homeostasis. These findings support the concept that pTA nanospheres mitigate oxidative stress through exogenous antioxidant buffering, thereby reducing the need for compensatory glutathione activity while maintaining a signalling-competent redox state. DCFDA staining exhibited a decrease in fluorescence intensity from 100 % (control) to approximately 40 % in pTA-treated cells (Fig. 6i–j), confirming that pTA effectively lowers oxidative stress.

On the other hand, confocal and STED super-resolution imaging of MDA-MB-231 cells stained for β -tubulin (green) and mitochondria (red) revealed marked alterations in both cytoskeletal and mitochondrial organisation in response to pTA nanospheres (Fig. 6k). In untreated cells, mitochondria were predominantly clustered around the nucleus, forming tight perinuclear aggregates associated with high ATP output and ROS generation. In contrast, pTA-treated cells exhibited more widely distributed microtubule networks that clearly outlined nuclear contours. Mitochondria were no longer centralized but instead extended along tubulin filaments toward the cell periphery, suggesting cytoskeleton-guided relocation away from the high-energy demand

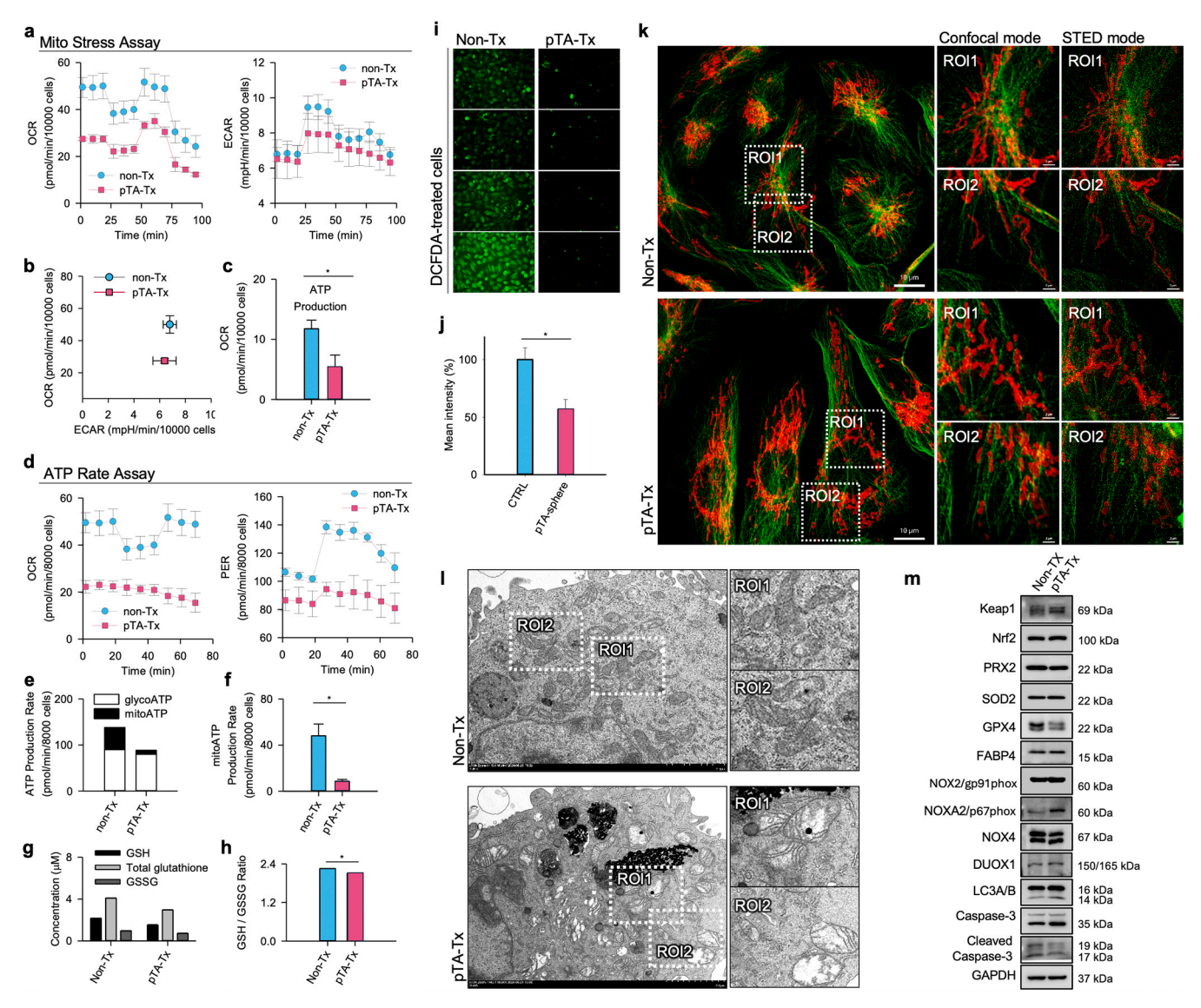


Fig. 6. pTA nanospheres modulate cellular metabolism and mitochondrial architecture. a Mito Stress Assay measuring oxygen consumption rate (OCR) and extracellular acidification rate (ECAR) over time. b OCR vs. ECAR scatter plot comparing metabolic phenotype under PTA treatment. c Bar graph showing ATP production-linked OCR (*p < 0.01). d ATP Rate Assay depicting OCR and proton efflux rate (PER) over time. e Total ATP production rate divided into glycolytic and mitochondrial contribution. f Quantified mitochondrial ATP production rate (*p < 0.01). Intracellular glutathione redox balance measurements: g GSH, total glutathione, and GSSG; h GSH/GSSG ratio (*p < 0.01). i ROS levels assessed by DCFDA fluorescence imaging in control vs. PTA-treated cells. j Quantification of mean DCFDA intensity (*p < 0.01). k Confocal and STED super-resolution imaging of cytoskeletal filaments (green: β-tubulin, red: mitochondria) showing two regions of interest (ROI) per condition. Scale bars mean 10 μm. l Transmission electron microscopy (TEM) of ultrastructural features in control and PTA-treated cells, highlighting regions of interest (ROI1 and ROI2). m Western blot for the indicated markers.

zone. High-magnification STED images further revealed thickened mitochondrial profiles in treated cells, suggesting swelling or hyperfusion. Such changes are often observed in response to altered redox conditions, with antioxidant environments favouring mitochondrial elongation or fusion as a stress adaptation mechanism. Mechanistically, pTA likely reduces intracellular ROS, thereby preventing mitochondrial fragmentation and supporting microtubule stabilization. This facilitates spatial repositioning of organelles and helps preserve mitochondrial function under metabolic duress. The redistribution and morphological changes observed may thus reflect a homeostatic adaptation aimed at reducing metabolic stress while maintaining organelle function under non-lethal conditions. Through redox regulation, pTA nanospheres remodel the mitochondrial-cytoskeletal interface, potentially impairing directional migration and altering metabolic dynamics in TNBC cells.

Transmission electron microscopy (TEM) provided ultrastructural evidence supporting redox-induced mitochondrial and metabolic

remodelling in response to pTA nanospheres [50]. In treated cells, mitochondria exhibited marked swelling, and electron-dense vesicular compartments were more abundant compared to the non-treated control (Fig. 61), consistent with a stress-adaptive phenotype. In particular, intracellular pTA nanosphere-like particles were clearly visible within the cytoplasm, suggesting successful uptake and intracellular localisation of the nanomaterial. Furthermore, the mitochondrial morphological changes observed by STED super-resolution imaging—specifically the increased thickness or diameter of individual mitochondria—were corroborated at the ultrastructural level by TEM, providing additional confirmation of organelle expansion. This mitochondrial swelling likely reflects impaired fission-fusion dynamics and is often associated with diminished respiratory efficiency. In addition, electron-dense pTA nanosphere-like structures were consistently found within membrane-bound vesicles, some of which exhibited double-membrane morphology suggestive of autophagosomes (Fig. S14). Although the precise co-localization with mitochondria or other organelles was not directly demonstrated, their proximity to organelle-rich regions supports the hypothesis that pTA nanospheres interact with subcellular compartments relevant to redox signaling. Together, these features align with the prior XF analysis results, wherein pTA treatment led to a pronounced reduction in oxidative phosphorylation-dependent ATP production. The observed mitochondrial alterations thus offer a structural basis for the bioenergetic deficits induced by redox-targeted nanotherapy in TNBC cells.

Complementary western blot analysis further substantiated the redox-driven stress adaptation induced by pTA nanospheres (Fig. 6m and Fig. S15). Antioxidant sensors and detoxifying enzymes (Keap1, Nrf2, PRX2, and SOD2) exhibited minimal changes upon treatment. Keap1 slightly increased while Nrf2 remained stable, suggesting that the canonical Keap1–Nrf2 axis was not strongly activated (Fig. S16) [51, 52]. Similarly, the peroxidases PRX2 and SOD2, which detoxify hydrogen peroxide, exhibited relatively stable expression, indicating that pTA treatment effectively limited intracellular ROS without triggering a strong compensatory upregulation of classical antioxidant enzymes. In contrast, GPX4 levels were substantially decreased, implying a lowered demand for lipid peroxide detoxification, possibly due to the antioxidant properties of pTA. FABP4, a lipid-binding protein often responsive to metabolic stress, remained unchanged, suggesting that lipid homeostasis was not significantly perturbed despite the redox shift.

Interestingly, the components of the NADPH oxidase complex displayed differential regulation. NOXA2 (p67phox) and DUOX1 were clearly elevated, while NOX2 expression slightly increased and NOX4 slightly decreased [53]. This pattern suggests a selective re-engagement of ROS-generating machinery, likely as a localized compensatory mechanism to preserve redox-sensitive signalling pathways in the context of globally reduced ROS. Such compartmentalized ROS signalling may support critical survival and adaptation functions without reinstating widespread oxidative damage. Markers of cell death and survival revealed a distinct shift away from apoptosis toward a cytostatic phenotype. Cleaved Caspase-3 remained barely detectable in pTA-treated cells, despite unchanged levels of total Caspase-3, indicating that classical apoptotic pathways were not activated. In contrast, a clear increase in LC3A/B conversion from LC3-I to LC3-II reflected autophagy induction, a non-lethal stress adaptation process that supports metabolic recycling and cellular maintenance energy-limited conditions [54].

To clarify the causal relationship between pTA-induced redox modulation and cytoskeletal disassembly, we performed a sequential recovery experiment under three conditions: untreated control (Non-Tx), pTA nanosphere treatment (pTA-Tx), and post-washout recovery (Recovery). In Fig. S17a, pTA-Tx induced a spread and flattened morphology with disrupted polarity, which was reversed upon serial passaging in normal medium, indicating phenotypic reversibility. Fig. S17b-c exhibits that cell viability was unaffected across all conditions, confirming the non-cytotoxic nature of the treatment. We further analyzed redox-regulatory pathways via Western blotting (Fig. S17d and Fig. S18), which revealed transient alterations in ROS-related enzymes (e.g., DUOX1, NOX2, GPX4) and autophagy markers (e.g., LC3A/ B) under pTA-Tx, all of which returned to baseline upon recovery. Crucially, cleaved Caspase-3 remained undetectable, supporting a nonapoptotic mode of action. These findings confirm that pTA nanospheres induce reversible redox reprogramming that regulates cytoskeletal organization through an adaptive, non-lethal mechanism.

Thus, these results demonstrate that pTA nanospheres promote a redox-reprogrammed cellular state characterized by suppression of global oxidative stress, preservation of localized redox signalling, and activation of autophagy rather than apoptosis. This mode of cyto-regulation corresponds with the observed inhibition of invasive behaviour and mechanical remodelling, positioning pTA nanospheres as promising modulators of tumour cell aggressiveness through redox-targeted strategies. These biochemical and biomechanical findings

align with the observed phenotypic alterations, including reduced adhesion, compromised cytoskeletal structure, spatial redistribution of MT1-MMP, and suppressed mitochondrial oxidative phosphorylation, demonstrating that pTA nanospheres induce a non-lethal remodelling program. This state appears to be sustained through autophagic turnover and spatially confined redox signalling, offering a compelling framework for non-apoptotic, anti-metastatic intervention in aggressive breast cancers. This state appears to be maintained through autophagic turnover and redox-modulated cytoskeletal remodelling, forming the basis for a promising non-apoptotic antimetastatic strategy. Thus, these coordinated responses impair the energetic and structural machinery necessary for invasive behaviour, supporting the therapeutic utility of redox-modulating nanomaterials in mechanoregulation-mediated suppression of metastasis.

4. Conclusions

We identify poly(tannic acid) (pTA) nanospheres, assembled entirely from tannic acid monomers, as effective intracellular antioxidants in TNBC cells. Beyond inhibiting proliferation, pTA treatment disrupted nuclear and cellular morphology, altered cytoskeletal architecture (Factin, vimentin), and redistributed MT1-MMP, a key protease in matrix degradation and invasion. These changes were accompanied by mitochondrial remodeling and reduced oxidative phosphorylation, highlighting redox-driven modulation of cellular mechanics and metabolism.

By leveraging a multimodal analytical approach encompassing highresolution imaging, spatial protease localization, metabolic profiling and ultrastructural analysis, we elucidated a mechanistic pathway through which redox modulation constrains invasive behavior. This in vitro analysis supports the potential of pTA nanospheres as redoxtargeted, anti-metastatic agents that modulate mechanical and biochemical cancer traits. To evaluate the broader applicability of this redox-driven mechanoregulatory mechanism, future studies will extend the platform to additional highly invasive TNBC cell lines (e.g., BT-549, MDA-MB-468) as well as distinct molecular subtypes of breast cancer (e. g., ER-positive, HER2-enriched models). This multilayered validation will elucidate whether the anti-invasive effects of pTA nanospheres are subtype-restricted or represent a generalizable therapeutic strategy across diverse oncogenic contexts. Before clinical translation, several challenges remain, including pTA stability in biological fluids, targeted delivery to tumor margins, and immune clearance. While tannic acid chemistry offers intrinsic biocompatibility, further preclinical studies are required to define the therapeutic window and delivery strategies. Altogether, our findings provide a foundation for developing redoxregulating nanomaterials that suppress metastasis by targeting the mechanical and metabolic vulnerabilities of invasive cancer cells.

Author Statement

This manuscript has not been submitted elsewhere, in part or its entirety, and is not under consideration by any other journal.

We did not use Generative AI and AI-assisted tools in Figures, images and artwork.

CRediT authorship contribution statement

Sungbaek Seo: Supervision. Suhui Jeong: Writing – review & editing, Writing – original draft, Visualization, Project administration, Methodology, Formal analysis, Data curation. Minhee Ku: Writing – review & editing, Writing – original draft, Project administration, Methodology, Investigation, Formal analysis. Hwain Myeong: Writing – review & editing, Visualization. Nara Yoon: Methodology, Data curation. Jaemoon Yang: Supervision. Jinwon Kwon: Writing – review & editing, Methodology, Data curation.

Declaration of Competing Interest

The authors declare that they have no known competing financial interests or personal relationships that could have appeared to influence the work reported in this paper.

Acknowledgments

This work was supported by the Technology Development Program (002792401) funded by the Ministry of SMEs and Startups (MSS, Korea) and a National Research Foundation of Korea (NRF) grant funded by the Ministry of Education, BK21 FOUR project (F21YY8109033) and the Ministry of Science and ICT (NRF-2020R1A2C1101616, NRF-2021R1A2C1009894, RS-2024-00440151), and a faculty research grant of Yonsei University College of Medicine (6-2024-0100)

Supporting Information

The online version contains supplementary material available at URL.

Appendix A. Supporting information

Supplementary data associated with this article can be found in the online version at doi:10.1016/j.nantod.2025.102907.

Data availability

Data will be made available on request.

References

- [1] X. Xu, W. Ho, X. Zhang, N. Bertrand, O. Farokhzad, Trends Mol. Med 21 (2015)
- [2] G. Shim, M.G. Kim, D. Kim, J.Y. Park, Y.K. Oh, Adv. Drug Deliv. Rev. 115 (2017)
- [3] A. Bardia, X. Hu, R. Dent, K. Yonemori, C.H. Barrios, J.A. O'Shaughnessy, H. Wildiers, J.-Y. Pierga, Q. Zhang, C. Saura, L. Biganzoli, J. Sohn, S.-A. Im, C. Lévy, W. Jacot, N. Begbie, J. Ke, G. Patel, G. Curigliano, N. Engl. J. Med. 391 (2024) 2110.
- [4] H. Hurwitz, L. Fehrenbacher, W. Novotny, T. Cartwright, J. Hainsworth, W. Heim, J. Berlin, A. Baron, S. Griffing, E. Holmgren, N. Ferrara, G. Fyfe, B. Rogers, R. Ross, F. Kabbinavar, Bevacizumab Irinotecan Fluor. Leucovorin Metastatic Colorectal
- [5] M. Xiao, L. Wang, Q. Tang, Q. Yang, X. Yang, G. Zhu, L. Lei, S. Li, VIEW 5 (2024).
- [6] S. George, H. Abrahamse, Antioxidants 9 (2020) 1.
- [7] M. Luo, L. Zhou, Z. Huang, B. Li, E.C. Nice, J. Xu, C. Huang, Antioxidants 11 (2022).
- [8] M. Jang, L. Cai, G.O. Udeani, K.V. Slowing, C.F. Thomas, C.W.W. Beecher, H.H. S. Fong, N.R. Farnsworth, A. Douglas Kinghorn, R.G. Mehta, R.C. Moon, J. M. Pezzuto, Cancer Chemopreventive Act. Resveratrol a Nat. Prod. Deriv. Grapes
- [9] X. Wu, Y. Tan, J. Zhang, R. Cui, C. Liao, S. Zhang, J. Mater. Chem. B 11 (2023)
- [10] J. Jung, M. Ku, S. Jeong, N. Yoon, J.H. Park, H.S. Youn, J. Yang, S. Seo, ACS Appl. Mater. Interfaces 15 (2023) 34462.
- [11] Q. Zhang, Y. Huang, R. Yang, J. Mu, Z. Zhou, M. Sun, Biomater. Sci. 10 (2022) 3637.
- [12] Z. Chen, Y. Liu, M. Lyu, C.H. Chan, M. Sun, X. Yang, S. Qiao, Z. Chen, S. Yu, M. Ren, A. Lu, G. Zhang, F. Li, Y. Yu, Cell Biosci. 15 (2025) 13.
- [13] K.A. Akshata Desai, Hered. Genet. (2013).

- [14] P. Zagami, L.A. Carey, NPJ Breast Cancer 8 (2022) 95.
- [15] M. Herrera Juarez, P. Tolosa Ortega, A. Sanchez de Torre, E. Ciruelos Gil, Breast Care 15 (2020) 208.
- [16] J. Wei, G. Wang, F. Chen, M. Bai, Y. Liang, H. Wang, D. Zhao, Y. Zhao, Angew. Chem. 130 (2018) 9986.
- [17] S. Jeong, S.Y. Kim, H. Myeong, E.K. Lim, S.M. An, H. Liang, K.K. Shrestha, M. S. Uddin, Y. Kim, P.I. Yi, B.S. An, S. Seo, ACS Omega (2024).
- [18] W. Stober, A. Fink, D.Ernst Bohn, Control. Growth Monodisperse Silica Spheres Micron Size Range 1 (1968).
- [19] J. Liu, T. Yang, D.W. Wang, G.Q. Lu, D. Zhao, S.Z. Qiao, Nat. Commun. 4 (2013).
- W. Cao, D. Li, S. Zhang, J. Ren, X. Liu, X. Qi, Arab. J. Chem. 16 (2023).
- [21] K. Liang, J.E. Chung, S.J. Gao, N. Yongvongsoontorn, M. Kurisawa, Adv. Mater. 30
- Y. Zhao, L. Xu, F. Kong, L. Yu, Chem. Eng. J. 416 (2021).
- J. Zhang, C.A. Peng, Biomater. Sci. 5 (2017) 2310.
- [24] J.P. Lewicki, C.A. Fox, M.A. Worsley, Polym. (Guildf.) 69 (2015) 45.
- [25] Z. Xia, W. Kiratitanavit, P. Facendola, S. Thota, S. Yu, J. Kumar, R. Mosurkal, R. Nagarajan, Polym. Degrad. Stab. 153 (2018) 227.
- [26] E. Tarani, M. Tara, C. Samiotaki, A. Zamboulis, K. Chrissafis, D.N. Bikiaris, Polym. (Basel) 16 (2024).
- [27] R. Bhomia, V. Trivedi, J.C. Mitchell, N.J. Coleman, M.J. Snowden, Ind. Eng. Chem. Res 53 (2014) 10820.
- [28] N. Sahiner, S. Sagbas, N. Aktas, Mater. Sci. Eng. C. 49 (2015) 824.
- [29] H. Zhang, Z. Yi, Z. Sun, X. Ma, X. Li, J. Mater. Chem. B 5 (2017) 7622.
- [30] F. Behboodi-Sadabad, H. Zhang, V. Trouillet, A. Welle, N. Plumeré, P.A. Levkin, Adv. Funct. Mater. 27 (2017).
- [31] C.-S.C. Woodcock, Y. Huang, S.R. Woodcock, S.R. Salvatore, B. Singh, F. Golin-Bisello, N.E. Davidson, C.A. Neumann, B.A. Freeman, S.G. Wendell, J. Biol. Chem. 293 (2018) 1120.
- [32] B. Xuan, D. Ghosh, E.M. Cheney, E.M. Clifton, M.R. Dawson, Sci. Rep. 8 (2018)
- [33] L.V. Bel'skaya, E.I. Dyachenko, Curr. Issues Mol. Biol. 46 (2024) 4646.
- [34] I.A. Kent, O. Zhang, A. Katiyar, Y. Li, S. Pathak, R.B. Dickinson, T.P. Lele, J. Cell Physiol. 234 (2019) 20675.
- [35] I. Thievessen, P.M. Thompson, S. Berlemont, K.M. Plevock, S.V. Plotnikov, A. Zemljic-Harpf, R.S. Ross, M.W. Davidson, G. Danuser, S.L. Campbell, C. M. Waterman, J. Cell Biol. 202 (2013) 163.
- [36] J. Sahana, T.J. Corydon, M. Wehland, M. Krüger, S. Kopp, D. Melnik, S. Kahlert, B. Relja, M. Infanger, D. Grimm, Front Cell Dev. Biol. 9 (2021).
- [37] M. Ku, J. Yang, Nano Converg. 10 (26) (2023).
- [38] Z. Liu, X. Zhang, T. Ben, M. Li, Y. Jin, T. Wang, Y. Song, Biomark. Res 13 (2025) 38.
- [39] J. Aseervatham, Biol. (Basel) 9 (2020) 385.
- [40] S. Kim, D.H. Kim, W. Lee, Y.-M. Lee, S.-Y. Choi, K. Han, Genom. Inf. 18 (2020) e35.
- [41] E.M. Wenzel, N.M. Pedersen, L.A. Elfmark, L. Wang, I. Kjos, E. Stang, L. Malerød, A. Brech, H. Stenmark, C. Raiborg, Nat. Commun. 15 (2024) 1277.
- [42] H. Lu, A.A. Bhat, D. Peng, Z. Chen, S. Zhu, J. Hong, S. Maacha, J. Yan, D. J. Robbins, M.K. Washington, A. Belkhiri, W. El-Rifai, Cancer Res 79 (2019) 4426.
- [43] R. Ferrari, G. Martin, O. Tagit, A. Guichard, A. Cambi, R. Voituriez, S. Vassilopoulos, P. Chavrier, Nat. Commun. 10 (2019) 4886. [44] N. Tanaka, T. Sakamoto, Cells 12 (2023) 2187.
- [45] C. Rossé, C. Lodillinsky, L. Fuhrmann, M. Nourieh, P. Monteiro, M. Irondelle, E. Lagoutte, S. Vacher, F. Waharte, P. Paul-Gilloteaux, M. Romao, L. Sengmanivong, M. Linch, J. van Lint, G. Raposo, A. Vincent-Salomon, I. Bièche, P.J. Parker, P. Chavrier, Proc. Natl. Acad. Sci. 111 (2014).
- [46] E.M. Grasset, M. Dunworth, G. Sharma, M. Loth, J. Tandurella, A. Cimino-Mathews, M. Gentz, S. Bracht, M. Haynes, E.J. Fertig, A.J. Ewald, Sci. Transl. Med 14 (2022).
- [47] K. Strouhalova, M. Přechová, A. Gandalovičová, J. Brábek, M. Gregor, D. Rosel, Cancers (Basel) 12 (2020) 184.
- [48] A. Bharadwaj, A. Kumar, S. Padalumavunkal Mathew, R. Mitra, J. Bhattacharyya, B.G. Jaganathan, B.R. Boruah, Biochem Biophys. Rep. 39 (2024) 101798.
- [49] C. Garcin, A. Straube, Essays Biochem 63 (2019) 509.
- [50] J. Kim, A. Park, J. Hwang, X. Zhao, J. Kwak, H.W. Kim, M. Ku, J. Yang, T.Il Kim, K.-S. Jeong, U. Choi, H. Lee, S.J. Shin, Cell Rep. 40 (2022) 111077.
- [51] Y.S. Lee, J. Kang, E.S. Jung, A. Lee, J. Breast Cancer 26 (2023) 461.
- [52] A.T. Al Haq, H.-Y. Tseng, L.-M. Chen, C.-C. Wang, H.-L. Hsu, Cell Death Dis. 13 (2022)49.
- N. Quilaqueo-Millaqueo, D.A. Brown-Brown, J.A. Vidal-Vidal, I. Niechi, Biol. Res 57 (2024) 98.
- [54] J. Debnath, N. Gammoh, K.M. Ryan, Nat. Rev. Mol. Cell Biol. 24 (2023) 560.